

# Online Measurement of Battery Impedance Using Motor Controller Excitation

David A. Howey, *Member, IEEE*, Paul D. Mitcheson, *Senior Member, IEEE*, Vladimir Yufit, Gregory J. Offer, and Nigel P. Brandon

**Abstract**—This paper presents a fast cost-effective technique for the measurement of battery impedance online in an application such as an electric or hybrid vehicle. Impedance measurements on lithium-ion batteries between 1 Hz and 2 kHz give information about the electrochemical reactions within a cell, which relates to the state of charge (SOC), internal temperature, and state of health (SOH). We concentrate on the development of a measurement system for impedance that, for the first time, uses an excitation current generated by a motor controller. Using simple electronics to amplify and filter the voltage and current, we demonstrate accurate impedance measurements obtained with both multisine and noise excitation signals, achieving RMS magnitude measurement uncertainties between 1.9% and 5.8%, in comparison to a high-accuracy laboratory impedance analyzer. Achieving this requires calibration of the measurement circuits, including measurement of the inductance of the current sense resistor. A statistical correlation approach is used to extract the impedance information from the measured voltage and current signals in the presence of noise, allowing a wide range of excitation signals to be used. Finally, we also discuss the implementation challenges of an SOC estimation system based on impedance.

**Index Terms**—Battery, condition monitoring, electric vehicle, hybrid vehicle, impedance spectroscopy, state of charge (SOC).

## I. INTRODUCTION

**E**LECTRIC and hybrid vehicles employ a battery management system (BMS) to monitor and control battery voltages, currents, and temperatures for safety reasons, and to calculate the battery state of charge (SOC), state of health (SOH) and other performance metrics. With respect to SOC, the most basic systems measure only steady-state values and use Coulomb counting, with an empirical model and lookup table of previously measured characteristic parameters to account for changes in performance at different charge and discharge rates

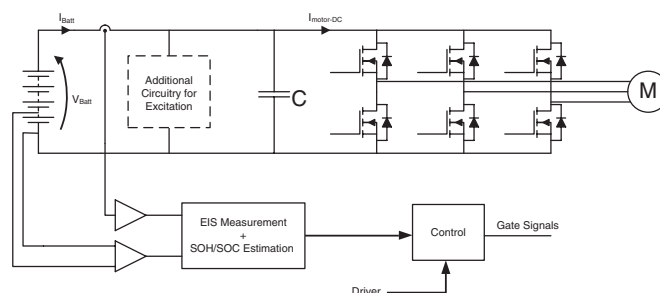


Fig. 1. Battery impedance measurement within vehicle drivetrain.

and with age [1]. More sophisticated systems use adaptive state estimation to fit parameters online, e.g., in [2] and [3].

Electrochemical impedance spectroscopy (EIS) is a powerful tool to investigate the fundamental electrochemical reactions occurring within cells. EIS measurements are obtained by varying the voltage and current of a cell at different frequencies to measure the impedance of the cell as a function of frequency. With accurate calibration and in combination with other methods, this technique can be used to gain vital information about the SOC and SOH of batteries, e.g., in [4]. Impedance measurement may be also used to detect and analyze faults in battery packs [5]. However, although EIS has been widely applied in the laboratory, it is a relatively specialized technique normally requiring expensive and bulky equipment to achieve accurate results [6]. There is growing interest in the use of EIS for “*in situ*” condition monitoring of batteries for a variety of applications. In this paper, our main goal is to demonstrate a low-cost but accurate excitation and measurement system for impedance that could be used online in a vehicle or other applications.

The overall system schematic of this paper is shown in Fig. 1 in relation to an electric-vehicle drive system. An impedance measurement system comprises an excitation system to perturb the cells, and a measurement and signal processing system to calculate the impedance. In our system, the excitation in a current comes either from variations in the main traction current due to driver or controller response, from an optional additional excitation circuit not discussed here, or from a combination of all of these. In this paper, we control both an electronic load and a motor controller to investigate these techniques. The electronic load was included since it allows a responsive and relatively low noise control of battery current. This enabled the development and verification of our hardware and signal processing approaches before moving to the much more challenging environment presented by a motor controller.

Manuscript received April 23, 2013; revised August 23, 2013 and October 14, 2013; accepted November 22, 2013. Date of publication December 3, 2013; date of current version July 10, 2014. This work was supported by the U.K. Engineering and Physical Sciences Research Council under Grant EP/H05037X/1. The review of this paper was coordinated by Dr. A. Davoudi.

D. A. Howey is with the Department of Engineering Science, University of Oxford, Oxford OX1 3PJ, U.K. (e-mail: david.howey@eng.ox.ac.uk).

P. D. Mitcheson is with the Department of Electrical and Electronic Engineering, Imperial College London, London SW7 2AZ, U.K.

V. Yufit is with the Department of Earth Science and Engineering, Imperial College London, London SW7 2AZ, U.K.

G. J. Offer is with the Department of Mechanical Engineering, Imperial College London, London SW7 2AZ, U.K.

N. P. Brandon is with the Energy Futures Lab, Imperial College London, London SW7 2AZ, U.K.

Color versions of one or more of the figures in this paper are available online at <http://ieeexplore.ieee.org>.

Digital Object Identifier 10.1109/TVT.2013.2293597

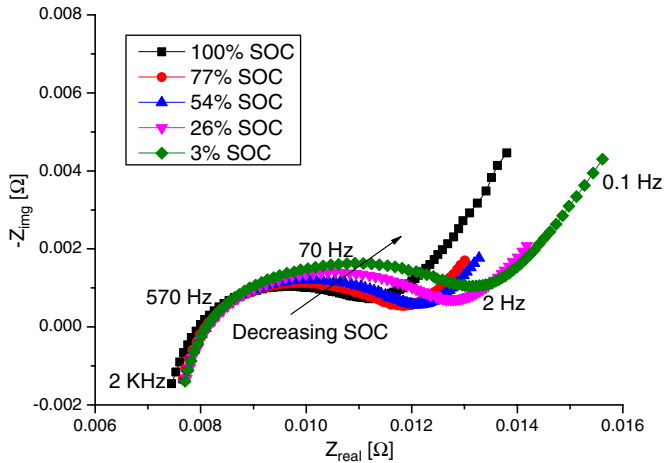


Fig. 2. Variation in LFP cell impedance with SOC ( $x$ -axis shows real part of impedance and  $y$ -axis shows negative reactive part).

The measurement and processing system consists of voltage and current measurement plus amplification and filtering, then digital processing to determine the cell's impedance as a function of frequency. Our focus here is to demonstrate a low-cost excitation and measurement system; therefore, we only briefly explore the implementation challenges of an impedance-based SOC estimation system as a first example of what could be inferred from impedance (see Section VI). In relation to this, Fig. 2 shows the measured variation in impedance with SOC for a lithium-ion iron phosphate (LFP) A123 Systems cell (ANR26650M1A, 2.3 Ah), which is obtained using a Bio-Logic VSP multichannel potentiostat and frequency response analyzer in galvanostatic mode with  $\pm 250$ -mA peak current fluctuations and zero dc. As shown, impedance varies with SOC and could, therefore, be used for direct SOC estimation. Cell temperature, SOH, and dc offset also affect the impedance and must be accounted for when using impedance to determine SOC.

Impedance spectroscopy is a useful tool for indirectly inferring SOC, but there is a noted lack of available equipment for on-vehicle impedance measurement [2]. Impedance spectra for lead-acid cells in stationary applications have been measured using naturally present system noise as the excitation [7], but this required a commercial laboratory impedance analyzer.

Bespoke current perturbation and impedance measurement circuitry for lead-acid cells was developed by Fairweather *et al.*, who demonstrated the use of pseudorandom binary sequences (PRBSs) as an excitation signal. The SOC and cold cranking (pulse discharge) capability of lead-acid cells have been shown to relate directly to impedance, and Bohlen *et al.* [8] and Blanke *et al.* [9] developed bespoke circuitry for the prediction of cold cranking capability using electrical noise present on the vehicle power bus.

The use of actively applied broadband noise to measure lithium-ion battery impedance by cross correlation of the voltage and current measurements was investigated by Christophersen *et al.* [10]. However, the results required extensive spectral averaging taking a number of minutes and were inconclusive as they exhibited some significant phase measurement error that highlights the difficulty in obtaining accurate results. They have since pursued an alternative approach using

multisine excitation with compensated synchronous detection and have several patents in this area (e.g., in [11]).

Considerable research has also focused on describing and modeling the impedance response of lithium-ion batteries under various conditions, which is necessary to develop an impedance-based BMS. Papers by Doyle *et al.* [12], who developed a mathematical model to simulate lithium battery impedance, and by Barsoukov *et al.* [13], who describe an impedance parameterization procedure, are relevant. Troltzsch *et al.* [4] showed that series resistance, charge transfer resistance, and the Warburg coefficient change significantly during battery aging. The use of voltage and current pulses occurring during normal vehicle operation to estimate internal resistance as a marker of battery aging was demonstrated by Remmlinger *et al.* [14]. Roscher *et al.* [15] show that the battery impedance increases with aging during high current pulses.

This brief review of the literature shows that there are relatively few examples of EIS being applied outside the laboratory, and there is a scope for development of this technique for direct online condition monitoring. However, a low-cost, simple, lightweight, but sufficiently accurate system is required.

There are significant challenges to overcome for the accurate measurement of battery impedance in automotive applications because the batteries exhibit extremely low impedance values (on the order of  $m\Omega$ ); therefore, the small-signal perturbation in voltage response is on the order of millivolts or less (see Fig. 6). In addition, the phase of the battery impedance is typically small, between  $-10^\circ$  and  $+10^\circ$ . Associated issues are 1) achieving a good SNR without causing the battery to behave nonlinearly, 2) ensuring a sufficiently fast measurement so that time invariance can be assumed, and 3) accurate measurement of absolute magnitude and phase of voltage and current. These challenges are explored in the remainder of this paper: in Section II, with respect to the first and second issues, and in Section III, with respect to the third issue.

## II. IMPEDANCE ESTIMATION TECHNIQUES

### A. Overview

Impedance measurement may be considered a form of system identification. With a sufficiently small current and voltage perturbation, the response of an electrochemical cell may be assumed linear. The small-signal current fluctuation  $i(t)$  is the system input and the resulting small-signal voltage fluctuation  $v(t)$  is the output, with the impedance being the system transfer function relating current to voltage, i.e.,

$$V(s) = Z(s)I(s) \quad (1)$$

where  $V(s)$  is the frequency-domain voltage signal,  $I(s)$  is the frequency-domain current signal, and  $Z(s)$  is the frequency-domain impedance. This is shown in Fig. 3, which also shows the addition of unknown uncorrelated output noise  $n(t)$  that is unavoidably measured together with the voltage response. For accurate measurement, the impact of this noise must be estimated. In practice, the signals are usually discrete time sampled; however, in this paper, we present the analysis in continuous time.

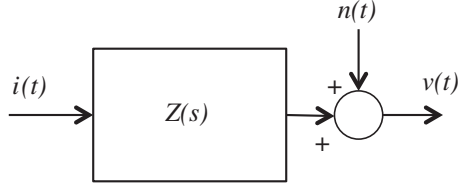


Fig. 3. Impedance represented as a transfer function.

A suitable excitation signal must be chosen, and signal processing algorithms are then used to extract the wanted impedance from the measurements in the presence of unwanted noise. A wide variety of common approaches are possible. We give a short overview of the four main approaches below to motivate and set in context our chosen approach described in Section II-E.

### B. Single-Sine-Frequency Sweep With Phase Detector

This is the most common approach used in electrochemical laboratories, with good noise rejection. However, it is relatively slow, and this can lead to nonsteady-state cell behavior during measurement. A persistent single-frequency sinusoidal current excitation  $i(t)$  is applied, and the voltage response  $v(t)$  is measured; this is then repeated at each frequency of interest, i.e.,

$$i(t) = I \cos(\omega t) \quad (2)$$

$$v(t) = V \cos(\omega t + \phi) \quad (3)$$

where  $I$  is the RMS current,  $V$  is the RMS voltage, and  $\phi$  is the phase difference between current and voltage. The impedance magnitude at the frequency  $\omega$  is given by the ratio  $V/I$ , and the phase  $\phi$  is calculated with a phase detector, which mixes the current with direct and quadrature voltage measurements and then low-pass filters the results to leave dc components proportional to the sine and cosine of  $\phi$ . To generate a high-quality pure sinusoid excitation signal required to implement this approach, a direct digital synthesis (DDS) chip can be used. Integrated solutions such as Analog Devices AD5933 provide the DDS, together with digital-to-analog and analog-to-digital converters and suitable processing.

### C. Multisine Excitation With Fourier Transforms

A number  $N$  of persistent concurrent multiple sinusoids at frequencies  $\omega_k$  may be applied as an excitation, i.e.,

$$i(t) = \sum_{k=1}^N \sin \omega_k t. \quad (4)$$

A windowed Fourier transform of the measured voltage and current can be used to calculate the impedance, i.e.,

$$\hat{Z}(\omega) = \frac{V(\omega)}{I(\omega)} \quad (5)$$

where  $V(\omega)$  is the Fourier transform of the voltage response, and  $I(\omega)$  is the Fourier transform of the current excitation signal. The estimated impedance  $\hat{Z}(\omega)$  is only valid at frequencies where  $I(\omega) \neq 0$ . A multisine excitation signal can be

synthesized using a digital signal processor and a digital-to-analog converter. A key consideration is that all frequencies  $\omega_k$  should be integer multiples of the lowest frequency to ensure periodicity. Moreover, the phases of the synthesized components must be randomized to normalize the total signal amplitude.

### D. Time-Domain Step Response With Fourier Transforms

The estimated impedance in response to an impulse magnitude  $\alpha$  is given by [16]

$$\hat{Z}(t) = \frac{v(t)}{\alpha}. \quad (6)$$

The estimate  $\hat{Z}$  in response to a step input is similar but with the derivative of  $v(t)$  as the numerator.

Impulse and step responses have the significant disadvantage that, due to the small impedance typical of batteries, the measured response  $v(t)$  is of small amplitude in comparison to the noise  $n(t)$ ; therefore, very large inputs are required for good SNR, which results in nonlinear behavior [16]. Further noise is introduced by differentiating  $v(t)$  for the step input case. Therefore, these approaches are not pursued further in this paper.

### E. Broadband Excitation With Stochastic Approaches

Here, our chosen method of signal processing is described. The frequency response of a system to a nondeterministic input signal may be computed by dividing the cross spectral density  $S_{iv}(\omega)$  between input and output signals by the input power spectral density  $S_{ii}(\omega)$ , i.e.,

$$\hat{Z}(\omega) = \frac{S_{iv}(\omega)}{S_{ii}(\omega)} \quad (7)$$

where, according to the Wiener–Khinchine theorem, the power spectral density of a wide-sense stationary signal is given by the Fourier transform of the autocorrelation function  $r_{ii}$ , i.e.,

$$S_{ii} = \int_{-\infty}^{\infty} r_{ii}(\tau) e^{-j\omega\tau} d\tau. \quad (8)$$

Similarly, the cross spectral density is given by the Fourier transform of the cross-correlation function  $r_{iv}$ , i.e.,

$$S_{iv} = \int_{-\infty}^{\infty} r_{iv}(\tau) e^{-j\omega\tau} d\tau \quad (9)$$

where the cross correlation (assuming ergodicity) is

$$r_{iv}(\tau) = \lim_{T \rightarrow \infty} \frac{1}{T} \int_{-T}^{+T} i(t) v(t + \tau) dt. \quad (10)$$

This approach is usually used with band-limited white noise as an excitation input signal. This may be generated using a random or pseudorandom number sequence, which may be prestored in a lookup table.

Similarly, PRBSs are repeating binary sequences that may be also used as excitation signals since, in the frequency domain,

they approximate band-limited white noise [17]. A PRBS may be pregenerated in software and stored in a lookup table. Both the bandwidth and the frequency resolution may be adjusted by adjusting the clock frequency and the number of stages in the PRBS generator. Full details may be found in [18].

To smooth a frequency response estimate measured with noise excitation, spectral averaging is used, i.e., convolution of  $\hat{Z}(\omega)$  with a window function such as a Hamming or Bartlett window. This reduces the estimate variance at the expense of introducing bias to the estimate. In our system, spectral averaging with a rolling average of ten data blocks was sufficient to obtain good-quality impedance data. Additionally, it is useful to truncate the estimated frequency response above some frequency; in our system, this frequency was 2 kHz.

The advantage of using a correlation-based approach is that a wide range of excitation signals may be used. However, one must distinguish between the desirable signal caused by the impedance and undesirable interference  $S_{nn}$ , which is added to the measurement at the system output (see Fig. 3), i.e.,

$$S_{vv} = |Z(\omega)|^2 S_{ii} + S_{nn}. \quad (11)$$

It is impossible to measure the magnitude of  $S_{nn}$  directly, but its impact may be estimated using the quadratic coherence spectrum, which returns a value between zero and one, as follows:

$$\gamma^2(\omega) = \frac{|S_{iv}(\omega)|^2}{S_{ii}(\omega)S_{vv}(\omega)}. \quad (12)$$

The coherence spectrum  $\gamma^2$  is a frequency-dependent correlation coefficient between two signals, which is useful both as a test of linearity and SNR. If  $\gamma^2 = 0$ , then  $i(t)$  and  $v(t)$  are unrelated, and if  $\gamma^2 = 1$ , then they are completely related by a linear transfer function. In practice, at each frequency,  $0 < \gamma^2 < 1$  due to the presence of undesired measurement noise, nonlinearity, or inputs, which have not been measured. The coherence function therefore gives a very useful method to remove poor-quality frequency response data. This may be achieved by ignoring data at frequencies where  $\gamma^2 < t_h$ , with  $t_h$  being a suitable coherence threshold, e.g.,  $t_h = 0.9$ .

Due to its flexibility and ability to reject interference, we selected the method described here for implementation. Our chosen approach for estimation of impedance is to use (7) to obtain  $\hat{Z}(\omega)$  from the time-domain measured voltage and current data, provided that  $\gamma^2(\omega) > t_h$  for each value of  $\omega$ . This was implemented in LabVIEW using standard library functions.

### III. EXPERIMENTAL SYSTEM

Here, we discuss the design and calibration of suitable measurement hardware to obtain the voltage and current measurements that may be used to estimate  $\hat{Z}(\omega)$  with the technique explained earlier.

#### A. Hardware Design

Two methods were used to excite the battery current: an electronic load (TTi LD300) with external control signal and

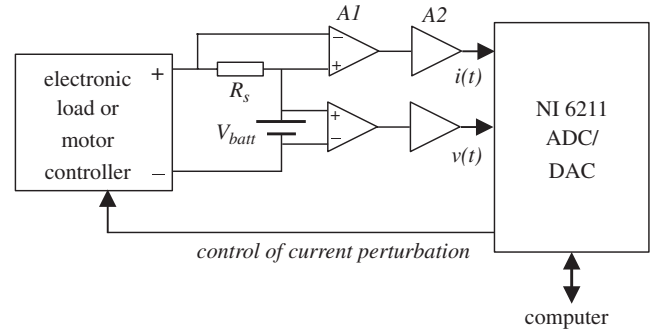


Fig. 4. Impedance measurement system for a single cell.

a motor controller (Elmo Piccolo) plus brushless permanent-magnet motor (Maxon EC 45) in current control mode. The approach using the motor drive is intended to demonstrate how this system might work in a vehicle application (see Section V). A National Instruments data acquisition system (NI 6211) was used for analog and digital input and output, which is controlled by a computer.

Fig. 4 shows the impedance measurement system built around the electronic load with current and voltage measurements. The measurement circuits consist each of a unity gain differential instrumentation amplifier A1 (Analog Devices AD627) followed by a passive  $RC$  high-pass filter plus non-inverting operational-amplifier gain stage A2 (Analog Devices OP97) configured for a gain of 100. The passive filter was chosen to have a low-frequency  $-3$  dB point around 1 Hz by selecting  $C \approx 12 \mu\text{F}$  and  $R \approx 10 \text{ k}\Omega$ , at which the phase shift is  $+45^\circ$ . The expected rolloff at low frequency is 20 dB/dec as this is a first-order filter. The reason for choosing this cutoff frequency was because we are interested in capturing impedance at relatively higher frequencies (around 10–2000 Hz for example) to make a fast measurement that does not interfere with other aspects of the end-use application and to avoid non-stationary battery behavior. These frequencies are sufficient to capture electric double layer, charge transfer, solid-electrolyte interphase (SEI) transport, inductance and series resistance effects in a battery, as well as some mass transport diffusion effects [19]. Accurate measurement of double-layer capacitance, charge transfer resistance, and series resistance, all of which are possible at these frequencies, may be used to indicate SOC, SOH, and temperature [20]. The current measurement circuit used a precision shunt resistor  $R_s$  combined with similar amplifiers as used on the voltage measurement circuit.

Both A1 and A2 have nonzero input offset voltages. The high-pass-filter stage ensures that any dc offset from A1 is removed; any dc offset from A2 is removed in software.

#### B. Calibration of Measurement Channels

The frequency response of each measurement channels will affect the measured results, but this can be compensated for, as described here, to achieve an accurate absolute measurement with low-cost equipment. Such an approach is preferable to using an expensive complex set of filters to achieve a flat frequency response. It was assumed throughout that all elements behave linearly. Calibration of the voltage and



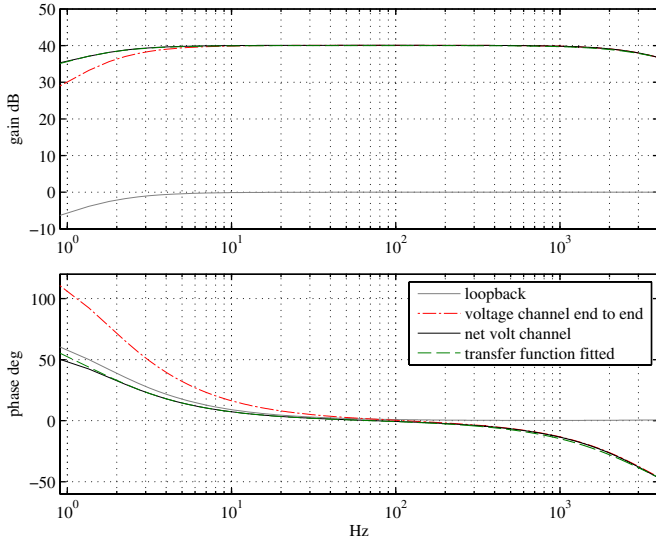


Fig. 5. Voltage channel measured response using a network analyzer.

current channels means that the individual accuracy of the resistors and capacitors in the circuit is not required to be known since the overall response is measured directly and then compensated for.

1) *Voltage Channel*: The voltage channel was characterized across a range of frequencies of interest (1 Hz–4 kHz) using an Audio Precision APX525 network analyzer, which applies a chirp voltage signal and measures the response. The loopback response of the wires connecting the circuit to the network analyzer was also measured separately and removed.

Fig. 5 shows the measured loopback response of the wires (gray), of the full voltage channel (A1 and A2, red, broken dashed), and of the net channel end-to-end response (black) with the loopback response removed. It was found that the loopback response of the cables was the same as the response of the instrumentation amplifier A1 (not shown separately in the figure) since this has unity gain and a very high gain–bandwidth product, although there is a small deviation in phase between 1 and 4 kHz likely caused by loopback cable inductance. Stage A2 introduces significant gain (40 dB) and has largely uniform magnitude response from 5 Hz to 1 kHz.

At low frequencies ( $< 100$  Hz), the net magnitude rolls off, and the phase increases due to the high-pass filter; at high frequencies ( $> 1$  kHz), the magnitude rolls off, and the phase decreases due to the low-pass filter formed around A2, which has a gain–bandwidth product of 400–500 kHz. With a gain of 100, the measured  $-3$ -dB point was at  $f = 3.77$  kHz. This forms an anti-aliasing filter, as the analog-to-digital converter samples at 20 kHz.

The overall combined response for the voltage measurement channel can be represented fairly accurately by the second-order transfer function, i.e.,

$$G_1(s) = \frac{1}{1 + s\tau_v} \frac{K_v s R_v C_v}{1 + s R_v C_v} \quad (13)$$

where  $\tau_v$  is the high-frequency  $-3$ -dB point,  $R_v$  is the value of the high-pass-filter resistor,  $C_v$  is the capacitor, and  $K_v$  is

the gain of A2. The response according to this transfer function is also shown in Fig. 5 (as a green dashed line); a small phase deviation is noted below 2 Hz and between 400 Hz and 3 kHz. For the greatest accuracy, the measured response data could be used instead of the fitted transfer function.

2) *Current Channel*: The current channel uses a 1%-precision  $0.1 \Omega$  shunt resistor (RS 363-6810) to produce a voltage drop proportional to the current. This is buffered by a differential amplifier, a high-pass filter, and a gain stage with the same design as A1 and A2, as already discussed for the voltage channel. The shunt-resistor temperature coefficient of resistance is  $-50$  to  $+100$  ppm per  $^\circ\text{C}$  [21]; therefore, a large temperature change of  $100^\circ\text{C}$  would be required to cause a resistance change of 1%. In our prototype system, the resistor dissipates small amounts of power (up to 25 mW), and this does not cause appreciable temperature change. In a vehicle application, the temperature stability of the current measurement sensor would need to be considered in a similar way to ensure that an accurate measurement is made. Alternative sensors such as current transducers may be used; these have appreciable inductance, and the calibration techniques outlined in this paper would need to be used to compensate for this.

Ideally, the current channel would have been calibrated by applying a known current signal and measuring the voltage response after A2. However, bench test equipment cannot drive very low impedance. Therefore, the shunt-resistor impedance was measured directly, and this was combined with the characterization of A1 and A2 in the same way as described for the voltage channel.

The shunt resistor behaves as a resistance in series with a small inductance and therefore has impedance given by

$$Z_s = R_s + sL_s \quad (14)$$

where  $Z_s$  is the shunt-resistor total impedance,  $R_s$  the resistance of the shunt, and  $L_s$  is the inductance, all in the frequency domain.

Using precision impedance measurement equipment (Bio-Logic VSP), it was found that  $R_s$  was very close to  $0.1 \Omega$  but that a small inductance  $\mu\text{H}$  was also present. Since

$$\angle Z_s = \tan^{-1} \left( \frac{\omega L_s}{R_s} \right) \quad (15)$$

$L_s$  can be therefore calculated from the phase response of the shunt resistor. In most other applications, this small inductance can be ignored, but for battery cells, as we have demonstrated for the first time in this paper, it cannot be ignored since it distorts the measured battery impedance at frequencies above a few hundred hertz.

Therefore, the response of the current measurement channel may be expressed using the following transfer function:

$$G_2(s) = \frac{1}{1 + s\tau_i} \frac{K_i s R_i C_i}{1 + s R_i C_i} (R_s + sL_s) \quad (16)$$

where, for the current channel,  $\tau_i$  is the high-frequency  $-3$ -dB point,  $R_i$  is the high-pass-filter resistor,  $C_i$  is the capacitor, and  $K_i$  is the gain of A2.

TABLE I  
CALIBRATION PARAMETERS FOR EXPERIMENTAL SYSTEM

$\tau_v$	2.37e4 rad/s	$K_v$	101.4
$R_v$	9.95 k $\Omega$	$C_v$	15.77 $\mu$ F
$\tau_i$	2.37e4 rad/s	$K_i$	101.4
$R_i$	9.95 k $\Omega$	$C_i$	15.79 $\mu$ F
$L_s$	4.2 $\mu$ H	$R_s$	0.1 $\Omega$

TABLE II  
TEST CELL INFORMATION [21]

Type	A123 Systems ANR26650
Dimensions (mm)	$\phi$ 26 x 65
Nominal capacity (Ah)	2.3
Nominal voltage (V)	3.3

In summary, the measured calibration parameters for the experimental system are given in Table I.

To apply the corrections to the estimated impedance  $\hat{Z}(\omega)$  obtained with (7) to find the calibrated impedance  $\hat{Z}_{cal}(\omega)$ ,  $\hat{Z}(\omega)$  is multiplied by  $G_2(s)/G_1(s)$  with  $s = j\omega$  at each frequency of interest as follows:

$$\hat{Z}_{cal}(\omega) = \hat{Z}(\omega) \frac{\frac{1}{1+s\tau_i} \frac{K_i s R_i C_i}{1+sR_i C_i} (R_s + sL_s)}{\frac{1}{1+s\tau_v} \frac{K_v s R_v C_v}{1+sR_v C_v}} \quad (17)$$

This calibrated impedance value may be then used for estimation of parameters such as SOC, as described in Section VI.

#### IV. RESULTS AND DISCUSSION USING ELECTRONIC LOAD

Using the TTI LD300 electronic load in current control mode, the impedance response of an A123 Systems LFP cell was measured using both a multisine excitation and broadband white noise excitation at ambient temperature conditions (between 18 °C and 21 °C). The specifications of the cell are given in Table II. Due to the unidirectional nature of current flow into the load, a constant dc offset condition was imposed on the cell. Therefore, test measurements were undertaken with  $I_{dc} = 150$  mA and a superimposed peak-to-peak perturbation  $I_{ac} = \pm 130$  mA. An example applied current perturbation from the electronic load and measured voltage response is shown in Fig. 6, where the waveform is comprised of 80 sinusoidal frequencies logarithmically spaced from 1 to 2000 Hz. The bode plot comparison from 0.1 Hz to 2 kHz with multisine excitation is given in Fig. 7, which also compares data obtained using a motor controller as excitation source (see Section V). In this figure, the approaches outlined in this paper are compared with a high-precision impedance measurement taken with a Bio-Logic VSP potentiostat system using the single-frequency sweep method and the same dc offset and peak-to-peak test conditions. Fig. 8 shows the same comparison but using broadband white noise as the excitation source instead. A summary of the uncertainty analysis for the electronic load data is given in Table III. The RMS uncertainty in magnitude is given by

$$\epsilon_{RMS} = \sqrt{\frac{1}{N} \sum_{k=1}^N [|Z_1(\omega_k)| - |Z_2(\omega_k)|]^2} \quad (18)$$

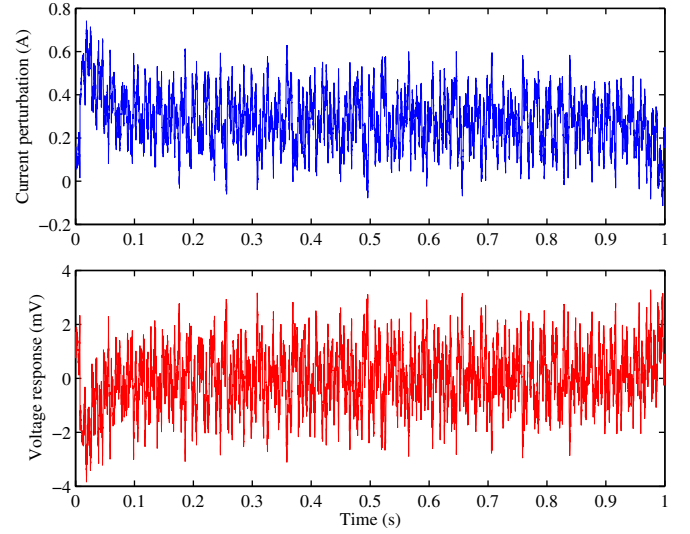


Fig. 6. Measured current and voltage of the single cell with multisine excitation.

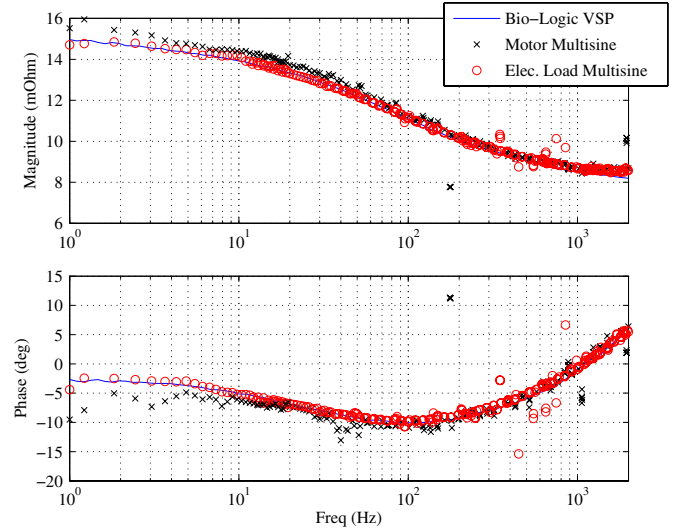


Fig. 7. Measured impedance comparison using multisine excitation.

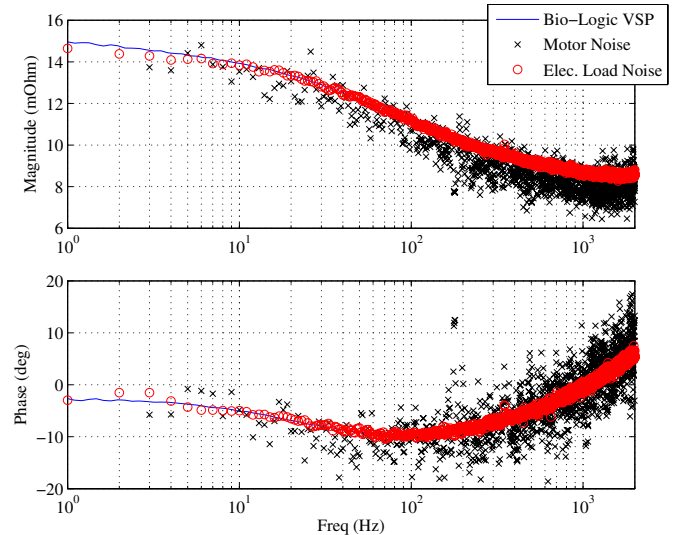


Fig. 8. Measured impedance comparison using broadband noise excitation.

TABLE III  
 UNCERTAINTY ANALYSIS OF ELECTRONIC LOAD DATA

Data set	$\epsilon_{RMS}$ (m $\Omega$ )	$\epsilon_{RMS}$ (%)	$\angle\epsilon_{RMS}$ ( $^\circ$ )
Multi-sine	0.23	2.6	1.2
Multi-sine without 50N Hz outliers	0.16	1.9	0.6
Noise	0.22	2.6	0.7

where subscript 1 indicates data from our system, and subscript 2 indicates data from the VSP potentiostat. Similarly, the RMS uncertainty in phase is given by

$$\angle\epsilon_{RMS} = \sqrt{\frac{1}{N} \sum_{k=1}^N [\angle Z_1(\omega_k) - \angle Z_2(\omega_k)]^2} \quad (19)$$

The percentage RMS uncertainty is calculated by dividing each absolute uncertainty by  $|Z_2|$  before taking the RMS. These uncertainties are rather crude estimates of the fit between the data sets, tending, for example, to penalize outliers heavily, but they indicate the accuracy of our approach.

The comparison between multisine electronic load measurements and the Bio-Logic VSP (see Fig. 7) is good across the full range of frequencies investigated (1 Hz–2 kHz) with RMS uncertainties of less than 3% in magnitude and less than 1.5° RMS phase uncertainty (see Table III). The multisine measurements exhibit outliers at odd harmonics of 50 Hz (the frequency of U.K. mains electricity). At these frequencies, there is a strong coherence ( $\gamma^2 > t_h$ ) between current and voltage [see (12)], but this is not caused by the battery impedance response; it is caused by narrow-band external interference to both the voltage and current measurements. The use of multisine excitation concentrates the energy in the excitation signal into a number of discrete frequencies, whereas broadband noise excitation spreads the energy across a wide range of frequencies. Therefore, the multisine results show increased sensitivity to narrow-band interference, in this case from mains electricity. Removing these outliers slightly improves the RMS uncertainty (see Table III).

The comparison between electronic load broadband noise measurements and Bio-Logic VSP (see Fig. 8) is also very good, exhibiting similar RMS uncertainties to the multisine case but with lower absolute phase uncertainty, demonstrating that this approach is less sensitive to narrow-band interference.

## V. RESULTS AND DISCUSSION USING MOTOR CONTROLLER

To explore the use of a vehicle motor controller as a variable current source and sink connected to excite a battery pack, a small test rig, which is shown in Fig. 9, was built and was comprised of a 30 W dc brushless servo motor (Maxon EC 45) with a motor controller (Elmo Piccolo), which was directly coupled to a second 30 W electrical machine (also Maxon EC 45) that was connected to the electronic load that is used to apply a dc load to the second electrical machine. The rig was powered by four A123 Systems LFP cells connected in series to form a 12–14 V dc supply. A steel flywheel with inertia

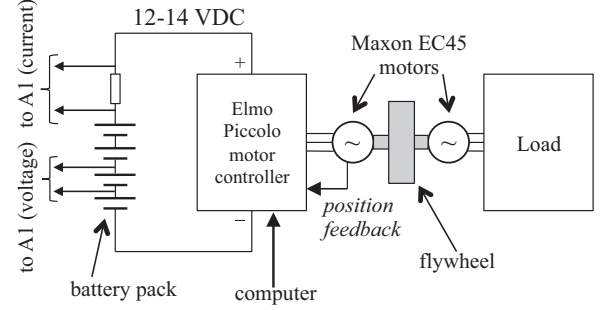


Fig. 9. Motor controller battery test system with four cells. Only one battery voltage measurement plus the current shunt is shown.

 TABLE IV  
 UNCERTAINTY ANALYSIS OF MOTOR RIG DATA

Data set	$\epsilon_{RMS}$ (m $\Omega$ )	$\epsilon_{RMS}$ (%)	$\angle\epsilon_{RMS}$ ( $^\circ$ )
Multi-sine	0.55	5.8	3.4
Multi-sine, without outliers	0.26	2.5	1.4
Noise	0.20	2.2	2.7

approximately  $0 > 15 \text{ g/m}^2$  was attached to the motor shafts to add mechanical energy storage and smooth speed fluctuations. The current fluctuations required to excite the battery result in torque fluctuations in the electrical machine, which result in small speed and position fluctuations. These are dampened by the flywheel as they would be also in a real vehicle application by the rotational inertia. The current fluctuations must be kept small to avoid significant torque ripple or problematic position errors. In our system, which used Hall sensors for position feedback, there were no problems with position errors or loss of control. In a real application, there will be a tradeoff between the maximum acceptable current fluctuation and the amount of averaging required to achieve a good SNR.

Since our primary interest is the use of the motor controller to impose current fluctuations on the battery pack, it is important to consider the closed-loop control bandwidth of the motor controller and the inductance of the motor coupled with the maximum bus voltage as these both limit the rate of change of battery current. In this case, the Elmo Piccolo motor controller has a maximum bandwidth of 3.2 kHz; thus, this is acceptable. The maximum rate of change of current is limited by the motor inductance and bus voltage, i.e.,

$$\frac{dI}{dt} = \frac{V}{L} \quad (20)$$

where  $L = 0.56 \text{ mH}$  for the motor used, and  $V \approx 12 \text{ V}$ ; therefore, the maximum  $dI/dt \approx 21\,429 \text{ A/s}$ . For a likely peak-to-peak current fluctuation of less than 500 mA, this gives a minimum half-cycle rise time of 23  $\mu\text{s}$ , i.e., a maximum frequency of around 21 kHz, which is also acceptable.

Using the motor test rig, both multisine and broadband noise excitation approaches were tested, and the results are shown in Figs. 7 and 8. A summary of uncertainty analysis data using the motor rig is given in Table IV using (18) and (19) to calculate the uncertainties.

In general, the RMS impedance magnitude uncertainties using the motor rig are similar but slightly larger than those using the electronic load particularly in the case of the multisine excitation, where there is narrow-band interference caused by the motor commutation. With noise excitation, the magnitude uncertainties are very similar and slightly better than using the electronic load. With both multisine and noise however, the motor rig shows greater phase uncertainty than the electronic load. Below 10 Hz, there is a deviation in both magnitude and phase caused by greater measurement noise and less averaging at these lower frequencies. Nonetheless, these results show that, in principle, a motor controller and very low cost measurement circuit could be used to excite a battery with broadband noise to measure its impedance magnitude with an RMS systematic uncertainty within 3% and RMS systematic phase uncertainty within  $3^\circ$  compared with an expensive precision laboratory tester.

## VI. TOWARDS ONLINE STATE-OF-CHARGE ESTIMATION

This paper has demonstrated that accurate impedance measurement may be carried out using an excitation current generated by a motor controller combined with a simple calibrated measurement circuit. Nonetheless, the eventual aim is to estimate SOC from impedance to supplement or replace other SOC estimation techniques such as Coulomb counting. Other metrics such as SOH may be also estimated, but we concentrate first on SOC. Initially, the impedance-based technique would be used during quiescent periods, for example, as part of a vehicle start-up process. This is to avoid large dc offset currents that change the battery equilibrium state with unknown consequences [20]. As more research is undertaken on the impact of dc on impedance response, our system could also be used under heavy loading.

In larger battery packs for electric vehicles, individual cell voltage monitoring is typically undertaken for safety reasons. The method described here may be therefore applied to individual series-connected cells. With parallel connected cells, voltage measurements for each individual cell cannot be decoupled; therefore, only the average impedance of a parallel set may be measured.

The approach described here using an electrical machine as the excitation system represents a scaled-down prototype of a brushless dc drive system. This is relevant as a demonstrator because of the relationship in the scaling of the relevant parameters as the drive system is increased in power: In a full-size electric vehicle, the battery packs will be larger, but so will the drive currents, and the perturbation current can be larger in absolute terms as the fraction of perturbation current to battery capacity can remain the same. For example, in our prototype, a peak-to-peak perturbation current of 150 mA on a 2.3 Ah capacity cell represents a C-rate of 0.07 C (where 1 C is the current required to fully discharge a cell in 1 h). In a real vehicle, for example, with battery pack capacity of 24 kWh and a voltage of 300 V, a perturbation current of 5.4 A peak would achieve approximately a 0.07 C-rate.

Small-signal equivalent circuit parameters such as series resistance  $R_0$  or double-layer capacitance usually represented

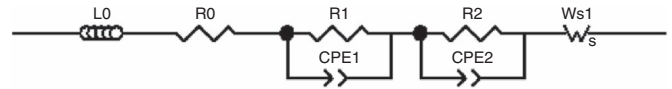


Fig. 10. LFP battery equivalent circuit.

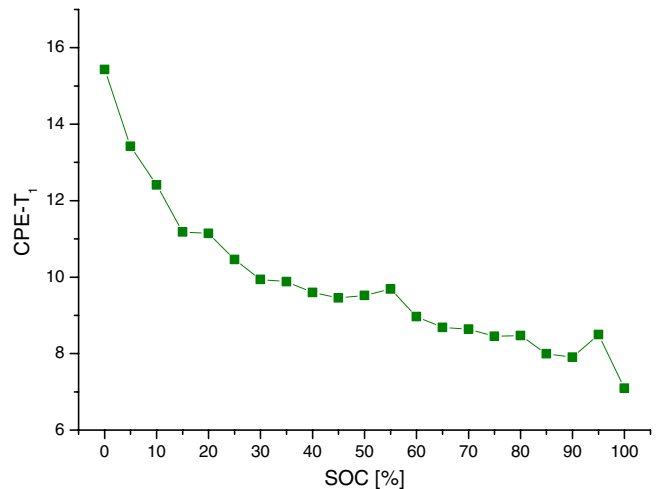


Fig. 11. CPE1 variation of admittance  $T_1$  with SOC.

using constant phase elements (CPEs) may be fitted to measured impedance using an optimization algorithm such as complex nonlinear least squares. A series of laboratory measurements relating parameters (extracted from impedance) to SOC and SOH must be taken beforehand. These would then be used in embedded hardware to estimate SOC and SOH from impedance. To investigate this approach, we have taken a series of measurements at various SOC and fitted parameters according to the equivalent circuit shown in Fig. 10, which includes two processes. The characteristic time constant of process 1 in the equivalent circuit is approximately 0.6 ms, and this process is related to lithium transport through the SEI, whereas process 2 with characteristic time constant of approximately 2 ms is related to charge transfer at the anode and the cathode [22]. In this circuit, CPEs are used rather than conventional capacitors since the former provide a better fit with real electrochemical devices that have a distributed range of dynamics rather than a fixed time constant. The CPE is defined as  $Z_{CPE} = 1/T(j\omega)^n$ ; for the case  $n = 1$ , this behaves as a conventional capacitor. From these data, the parameter showing the greatest variation with SOC for the A123 Systems LFP cells is the CPE parameter  $T_1$ , which shows a 2:1 variation across the range of SOC (see Fig. 11). In contrast, other parameters such as the high-frequency series resistance  $R_0$  vary only by around 10% or less over the range of SOC. However, in practice, for LFP cells, a combination of more than one parameter would need to be used for SOC estimation because the relationship between the parameters and SOC is not monotonic for this chemistry.

For other lithium-ion chemistries such as nickel–manganese–cobalt oxide (NMC), there is a clear monotonic parameter variation with SOC, as shown in Fig. 12, which shows the impedance variation with SOC for a Kokam 4.8 Ah prismatic NMC cell (SLPB 11043140H) at various SOC and ambient temperature, and in Fig. 13, which shows the variation in  $R_1$  and  $R_2$ , i.e., the resistances related to the SEI and charge



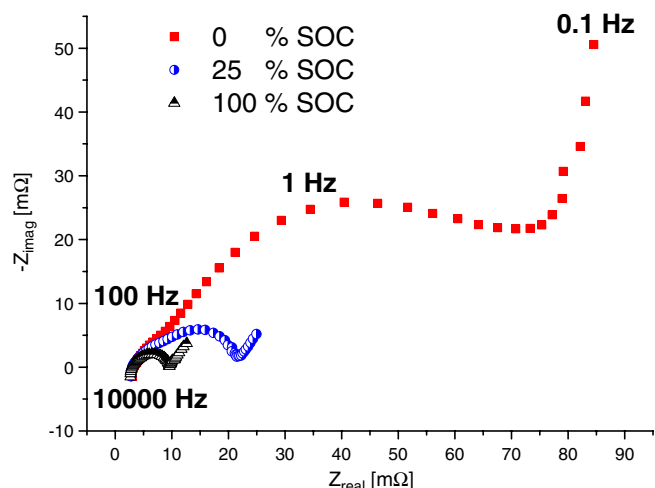
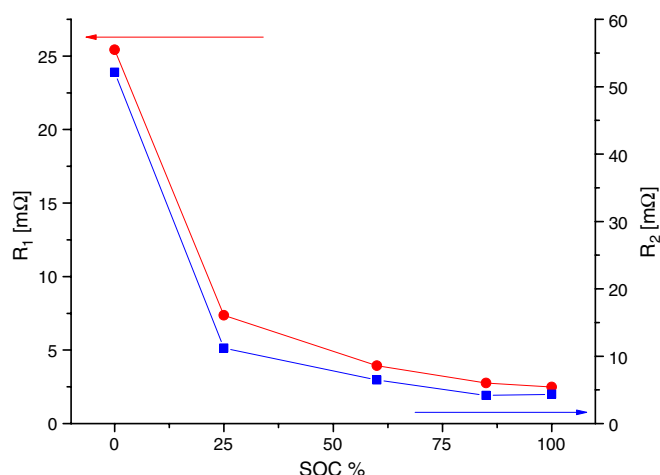


Fig. 12. NMC cell impedance variation with SOC.


 Fig. 13. SEI resistance  $R_1$  and charge transfer resistance  $R_2$  variation with SOC for the NMC cell.

transfer processes, respectively, as explained earlier. These were fitted to the impedance data using the same equivalent circuit model as the LFP cell.

## VII. CONCLUSION

This paper has demonstrated a cost-effective battery impedance measurement system that could be used online in an application to measure impedance accurately at a range of frequencies of interest using the existing power electronics as the excitation source. A number of conclusions may be drawn.

The first is the importance of accounting for unwanted noise in the signal processing and using the coherence spectrum to estimate such noise to ignore poor quality data. On the other hand, broadband noise can in fact be used as a suitable excitation signal to measure impedance, and it may, therefore, be possible to measure impedance using noise already present in an application. Broadband noise excitation also has the advantage of being relatively immune to narrow-band interference.

A second conclusion is the importance of accurate calibration of the voltage and current measurement channels to amplify the signals and remove any distorting effects from

the measurement circuits. A straightforward procedure was demonstrated to characterize the measurement channels and fit their frequency responses with appropriate transfer functions. The effect of current shunt-resistor inductance is noteworthy, and this inductance must be measured and compensated for.

Lowest RMS uncertainties between measured impedance magnitude and laboratory benchmark equipment were achieved using multisine perturbation preprocessed to remove narrow-band outliers due to mains frequency interference and motor commutation. However, both multisine and broadband noise signals could be used for impedance measurement, together with a suitable parameter estimation optimization algorithm.

Finally, we discussed the implementation challenges of SOC estimation from impedance in both LFP and NMC cells, concluding that, for the former SOC, estimation would be challenging and a combination of fitted parameters would need to be used, whereas for the latter, there are clear monotonically varying parameters from which SOC may be estimated.

## ACKNOWLEDGMENT

The authors would like to thank B. Wu of the Imperial College London, London, U.K. for recording the EIS data for the NMC cell.

## REFERENCES

- [1] E. Meissner and G. Richter, "Battery monitoring and electrical energy management: Precondition for future vehicle electric power systems," *J. Power Sources*, vol. 116, no. 1/2, pp. 79–98, Jul. 2003.
- [2] G. Plett, "Extended kalman filtering for battery management systems of LiPB-based HEV battery packs, Part 1: Background," *J. Power Sources*, vol. 134, no. 2, pp. 252–261, Aug. 2004.
- [3] D. V. Do, C. Forgez, K. El Kadri Benkara, and G. Friedrich, "Impedance observer for a Li-Ion battery using Kalman filter," *IEEE Trans. Veh. Technol.*, vol. 58, no. 8, pp. 3930–3937, Oct. 2009. [Online]. Available: <http://ieeexplore.ieee.org/lpdocs/epic03/wrapper.htm?arnumber=5184857>
- [4] U. Troltzsch, O. Kanoun, and H. Trankler, "Characterizing aging effects of lithium ion batteries by impedance spectroscopy," *Electrochimica Acta*, vol. 51, no. 8/9, pp. 1664–1672, Jan. 2006.
- [5] G. J. Offer, V. Yufit, D. A. Howey, B. Wu, and N. P. Brandon, "Module design and fault diagnosis in electric vehicle batteries," *J. Power Sources*, vol. 206, pp. 383–392, May 2012. [Online]. Available: <http://linkinghub.elsevier.com/retrieve/pii/S0378775312001863>
- [6] L. Lu, X. Han, J. Li, J. Hua, M. Ouyang, and Y. Zheng, "A review on the key issues for lithium-ion battery management in electric vehicles," *J. Power Sources*, vol. 226, pp. 272–288, Mar. 2013.
- [7] R. Robinson, "System noise as a signal source for impedance measurements on batteries connected to operating equipment," *J. Power Sources*, vol. 42, no. 3, pp. 381–388, Feb. 1993.
- [8] O. Bohlen, S. Buller, R. De Doncker, M. Gelbke, and R. Naumann, "Impedance based battery diagnosis for automotive applications," in *Proc. IEEE 35th Annu. Power Electron. Spec. Conf.*, 2004, pp. 2792–2797.
- [9] H. Blanke, O. Bohlen, S. Buller, R. Dedoncker, B. Fricke, A. Hammouche, D. Linzen, M. Thele, and D. Sauer, "Impedance measurements on lead acid batteries for state-of-charge, state-of-health and cranking capability prognosis in electric and hybrid electric vehicles," *J. Power Sources*, vol. 144, no. 2, pp. 418–425, Jun. 2005.
- [10] J. P. Christophersen, C. G. Motloch, J. L. Morrison, I. B. Donnellan, and W. H. Morrison, "Impedance noise identification for state-of-health prognostics," presented at the 43rd Power Sources Conf., Philadelphia, PA, USA, 2008, INL/CON-08-14101.
- [11] J. Morrison, W. Morrison, and J. Christophersen, "Method of detecting system function by measuring frequency response," U.S. Patent 20 100 274 510, Oct. 2010.
- [12] M. Doyle, J. P. Meyers, and J. Newman, "Computer simulations of the impedance response of lithium rechargeable batteries," *J. Electrochem. Soc.*, vol. 147, no. 1, p. 99, 2000.

- [13] E. Barsoukov, J. H. Kim, D. H. Kim, K. S. Hwang, C. O. Yoon, and H. Lee, "Parametric analysis using impedance spectroscopy: Relationship between material properties and battery performance," *J. New Mater. Electrochem. Syst.*, vol. 3, pp. 303–310, 2000.
- [14] J. Remmlinger, M. Buchholz, M. Meiler, P. Bernreuter, and K. Dietmayer, "State-of-health monitoring of lithium-ion batteries in electric vehicles by on-board internal resistance estimation," *J. Power Sources*, vol. 196, no. 12, pp. 5357–5363, Jun. 2011.
- [15] M. A. Roscher, J. Assfalg, and O. S. Bohlen, "Detection of utilizable capacity deterioration in battery systems," *IEEE Trans. Veh. Technol.*, vol. 60, no. 1, pp. 98–103, Jan. 2011. [Online]. Available: <http://ieeexplore.ieee.org/lpdocs/epic03/wrapper.htm?arnumber=5613947>
- [16] L. Ljung, *System Identification: Theory for the User*, 2nd ed. Englewood Cliffs, NJ, USA: Prentice-Hall, 1999.
- [17] A. Fairweather, M. Foster, and D. Stone, "VRLA battery parameter identification using pseudo random binary sequences (PRBS)," in *Proc. 5th IET Int. Conf. PEMD*, 2010, pp. TU244-1–TU244-6.
- [18] J. Schwarzenbach and K. Gill, *System Modelling and Control*, 3rd ed. London, U.K.: Edward Arnold, 1991.
- [19] A. Jossen, "Fundamentals of battery dynamics," *J. Power Sources*, vol. 154, no. 2, pp. 530–538, Mar. 2006. [Online]. Available: <http://linkinghub.elsevier.com/retrieve/pii/S0378775305014321>
- [20] W. Waag, S. Käbitz, and D. U. Sauer, "Experimental investigation of the lithium-ion battery impedance characteristic at various conditions and aging states and its influence on the application," *Appl. Energy*, vol. 102, pp. 885–897, Feb. 2012. [Online]. Available: <http://linkinghub.elsevier.com/retrieve/pii/S030626191200671X>
- [21] *Nanophosphate High Power Lithium Ion Cell ANR26650M1-B Data Sheet*, A123, Waltham, MA, USA, 2011. [Online]. Available: <http://info.a123systems.com/data-sheet-26650-cylindrical-cell>
- [22] T. K. Dong, A. Kirchev, F. Mattera, and Y. Bultel, "Modeling of lithium iron phosphate batteries by an equivalent electrical circuit: Method of model parameterization and simulation," *ECS Trans.*, vol. 25, no. 35, pp. 131–138, 2010. [Online]. Available: <http://ecst.ecsdl.org/cgi/doi/10.1149/1.3414011>



**David A. Howey** (M'10) received the B.A. and M.Eng. degrees from Cambridge University, Cambridge, U.K., in 2002 and the Ph.D. degree from Imperial College London, London, U.K., in 2010.

He is currently a Lecturer with the Energy and Power Group, Department of Engineering Science, University of Oxford, Oxford, U.K. He leads projects on fast electrochemical modeling, model-based battery management systems, battery thermal management, and motor degradation. His research interests include condition monitoring and management of

electric-vehicle components.



**Paul D. Mitcheson** (M'02–SM'12) received the M.Eng. and Ph.D. degrees from Imperial College London, London, U.K., in 2001 and 2005, respectively.

He is currently a Senior Lecturer with the Control and Power Research Group, Department of Electrical and Electronic Engineering, Imperial College London. His research interests include power electronics across various scales, from energy harvesting to high-voltage direct current, and interfaces for inductive power transfer. He has a parallel stream of

work on *in situ* battery status monitoring.



**Vladimir Yufit** received the Ph.D. degree from Tel Aviv University, Tel Aviv, Israel, leading pioneering work on development of 3-D thin-film lithium-ion microbatteries.

He is a Postdoctoral Research Associate with the Department of Earth Science and Engineering, Imperial College London, London, U.K. His research interests include rechargeable nonaqueous batteries; polymer electrolyte membrane, alkaline, and solid oxide fuel cells; redox flow batteries and regenerative fuel cells; supercapacitors; and advanced characteri-

zation techniques.



**Gregory J. Offer** received the M.Sci. and Ph.D. degrees from Imperial College London, London, U.K., in 2001 and 2007, respectively.

He is currently a Lecturer of mechanical engineering with the Department of Mechanical Engineering, Imperial College London, London, U.K., where he also holds an Engineering and Physical Sciences Research Council Career Acceleration Fellowship. He is also an electrochemist, working at the interface between the fundamental science and systems engineering of fuel cells, batteries, and supercapacitors.

His research interests include the degradation and failure of such components in automotive applications and the impact on system design and *vice versa*.



**Nigel P. Brandon** received the B.Eng. and Ph.D. degrees from Imperial College London, London, U.K., in 1981 and 1984, respectively.

He is currently a Director of the Energy Futures Lab, Imperial College London, London, U.K. His research interests include the science and engineering of electrochemical power sources, with a particular focus on batteries and fuel cells.

Mr. Brandon is an Officer of the Most Excellent Order of the British Empire and a Fellow of the Royal Academy of Engineering.